



HAL
open science

High-finesse Fabry-Perot cavities with bidimensional Si_3N_4 photonic-crystal slabs

X Chen, C Chardin, K Makles, C Caër, S Chua, R Braive, I Robert-Philip, T Briant, P.-F Cohadon, A Heidmann, et al.

► **To cite this version:**

X Chen, C Chardin, K Makles, C Caër, S Chua, et al.. High-finesse Fabry-Perot cavities with bidimensional Si_3N_4 photonic-crystal slabs. 2016. hal-01291712v2

HAL Id: hal-01291712

<https://hal.science/hal-01291712v2>

Preprint submitted on 1 Jun 2016

HAL is a multi-disciplinary open access archive for the deposit and dissemination of scientific research documents, whether they are published or not. The documents may come from teaching and research institutions in France or abroad, or from public or private research centers.

L'archive ouverte pluridisciplinaire **HAL**, est destinée au dépôt et à la diffusion de documents scientifiques de niveau recherche, publiés ou non, émanant des établissements d'enseignement et de recherche français ou étrangers, des laboratoires publics ou privés.

Public Domain

High-finesse Fabry-Perot cavities with bidimensional Si_3N_4 photonic-crystal slabs

X. Chen,¹ C. Chardin,¹ K. Makles,¹ C. Caër,^{1,*} S. Chua,¹ R. Braive,^{2,3} I. Robert-Philip,²
T. Briant,¹ P.-F. Cohadon,¹ A. Heidmann,¹ T. Jacqmin,¹ and S. Deléglise¹

¹*Laboratoire Kastler Brossel, UPMC-Sorbonne Universités, CNRS, ENS-PSL Research
University, Collège de France, 4 place Jussieu, Case 74, F75252 Paris Cedex 05, France*

²*Laboratoire de Photonique et de Nanostructures LPN-CNRS/CNRS, Route de Nozay, 91460 Marcoussis, France*

³*Université Paris Diderot, Sorbonne Paris Cité, 75207 Paris Cedex 13, France*

(Dated: June 1, 2016)

ABSTRACT

Light scattering by a two-dimensional photonic crystal slab (PCS) can result in dramatic interference effects associated with Fano resonances. Such devices offer appealing alternatives to distributed Bragg reflectors or filters for various applications such as optical wavelength and polarization filters, reflectors, semiconductor lasers, photodetectors, bio-sensors, or non-linear optical components. Suspended PCSs also find natural applications in the field of optomechanics, where the mechanical modes of a suspended slab interact via radiation pressure with the optical field of a high finesse cavity. The reflectivity and transmission properties of a defect-free suspended PCS around normal incidence can be used to couple out-of-plane mechanical modes to an optical field by integrating it in a free space cavity. Here, we demonstrate the successful implementation of a PCS reflector on a high-tensile stress Si_3N_4 nanomembrane. We illustrate the physical process underlying the high reflectivity by measuring the photonic crystal band diagram. Moreover, we introduce a clear theoretical description of the membrane scattering properties in the presence of optical losses. By embedding the PCS inside a high-finesse cavity, we fully characterize its optical properties. The spectrally, angular, and polarization resolved measurements demonstrate the wide tunability of the membrane's reflectivity, from nearly 0 to 99.9470 ± 0.0025 %, and show that material absorption is not the main source of optical loss. Moreover, the cavity storage time demonstrated in this work exceeds the mechanical period of low-order mechanical drum modes. This so-called resolved sideband condition is a prerequisite to achieve quantum control of the mechanical resonator with light.

INTRODUCTION

Fano resonances resulting from the interference between a discrete resonance and a broadband continuum of

states are ubiquitous in physical science and constitute a unique resource in the field of nanophotonics [1]. The scattering properties of subwavelength periodic structures can be tailored by engineering their asymmetric Fano lineshapes. These extraordinary and controllable optical properties hold great promise in the context of nanophotonics, where fully integrated Photonic Crystal Slabs (PCS) can replace traditional Bragg multi-layers for various optical components. This approach was already successfully implemented in the context of optical filters [2], switches [3], sensors [4], lasers [5], slow-light [6] and non-linear devices [7]. It was also proposed as a possible route to reduce thermal noise in the mirrors of large-scale gravitational-wave interferometers [8].

Moreover, nanophotonics is playing an increasing role in the field of optomechanics, by allowing sub-micron-scale mechanical resonators to interact via radiation pressure with highly confined optical fields. A very successful approach consists in colocalizing a photonic and a phononic mode in the small volume of a defect cavity in the plane of a PCS [9, 10]. In this setup, the mechanical resonator consists in a GHz internal vibrational mode localized in a very small mode volume around the defect cavity. More recently, defect-free suspended PCS have been used as lightweight mirrors of submicron thickness [11–13]. The out-of-plane vibrational modes of the membrane can be coupled to an optical field by integrating the membrane inside a high finesse cavity. Because of their very low mass and low mechanical frequency in the MHz range, such resonators are highly susceptible to radiation pressure. Moreover, they are good candidates to realize hybrid opto-electro-mechanical transducers [14, 15] as the out-of-plane vibrational modes of a suspended PCS can be simultaneously coupled to a nearby interdigitated capacitor. Such a device could play a decisive role in future (quantum) information networks as it allows to up-convert microwave signals onto an optical carrier for subsequent detection or transmission into optical fibers.

Suspended membranes made from thin layers of highly stressed materials are an advantageous platform for the development of optomechanical PCS as they present excellent mechanical properties [16]. For instance, recent experiments have demonstrated Q-factors exceeding 10^8 with high stress Si_3N_4 films at room [17, 18] and cryogenic [19] temperatures. Moreover, on the optical side, a

stringent requirement is the so-called resolved sideband (or good cavity) limit [20] in which the cavity storage time exceeds the mechanical period. To date, PCS optomechanical resonators have been demonstrated with 1D periodic patterns (often referred to as High Contrast Grating) [11, 21] or 2D photonic crystal patterns [12, 13, 18] that are insensitive to the incident polarization and that preserves the mechanical stiffness of the membrane. However, in these experiments, the PCS structures were suffering from a low optical reflectivity, precluding the operation in the resolved sideband regime and in most cases, the PCS was fabricated in a low tensile stress material, preventing from reaching high mechanical quality factors.

Here, we report on the implementation and full optical characterization of a PCS directly etched on a high tensile stress 200 nm-thick Si_3N_4 nanomembrane. We have reached the resolved sideband condition for the first time with a PCS used as the end-mirror of a Fabry-Perot cavity. The cavity finesse, of 6385 ± 150 is, to the best of our knowledge, an unprecedented value with free-space PCS cavities. The inferred membrane reflectivity is given by $1 - R = 530 \pm 25$ ppm. Moreover, we measured the band diagram of the guided resonances responsible for the Fano resonances in the PCS with an angle resolved spectrometer. In contrast with previous works conducted in the context of PCS optical filters [22] and reflectors [23], we give a physical interpretation of the observed band diagram and shed new light on the physics of these structures. Finally, we introduce a theoretical description of the scattering properties of the PCS in the presence of optical losses and demonstrate that the current reflectivity is not yet limited by material absorption. Demonstrating high-reflectivity PCS in a high-tensile stress film such as Si_3N_4 as evidenced here could also be beneficial in fields different from optomechanics, such as generation of tunable optical filters [24] or optomechanical lasers [5].

METHODS

A. Membrane and photonic crystal fabrication

The commercial membranes [25] are made of a 200 nm stoichiometric Si_3N_4 film deposited on a Si substrate and released over a 1 mm \times 1 mm square by chemical etching of the substrate (see Fig. 1a). High tensile stress in the film ensures mechanical modes with quality factors as high as 10^8 at low temperature [19] and ultra-low mass [26]. The photonic crystal is realized in the centre of the membrane. It is obtained by electron-beam lithography on a layer of 200 nm of Poly(methyl methacrylate) (PMMA) resist, followed by reactive ion etching with a plasma of CHF_3 and SF_6 . The PMMA is then stripped off with an oxygen plasma. The photonic crystal consists of a 270- μm diameter disk patterned with a square lat-

tice of circular holes (see Fig. 1). The lattice parameter is $\Lambda = 830$ nm, and the design value for the hole radius is 293 nm.

B. PCS characterization

Band diagram measurement

We implemented the white-light illumination and imaging setup shown in Fig. 2(a) to measure the PCS band diagram. A halogen white lamp is combined with a set of 3 lenses (L_1, L_2, L_3) and two diaphragms (D_1, D_2) to realize a Köhler illumination configuration. A field diaphragm (D_1) conjugated to the PCS restricts the illumination to the PCS area thus reducing the impact of light scattered on optical elements and mounts. The aperture diaphragm (D_2) is used to select the incident beam angles at the PCS position. It is centred on the optical axis and its aperture width is chosen to reject high angle-of-incidence components that are irrelevant for this experiment. A magnified image of the PCS is obtained with a microscope objective (L_4) and a lens (L_5). At the image plane sits a field diaphragm (D_3), conjugated to diaphragm (D_1), providing additional filtering of unwanted scattered light. A fiber tip is positioned in the focal plane of lens (L_6), that is in the Fourier plane of this imaging system. The light collected by the fiber is guided to a near-infrared spectrometer. By scanning the fiber in the transverse (x, y) plane the transmission spectrum can be measured at different angles. Moreover, a polarizer (Pol) is introduced between (L_1) and (L_2) for polarization selection.

PCS reflection, transmission and losses measurements

We implemented a single-ended cavity with the PCS as the end-mirror (Fig. 2b) to characterize its reflectivity, transmission and losses. The input mirror of the cavity is a 20 mm radius-of-curvature mirror and the cavity length is 17.4 mm. This ensures a waist size $w_0 = 48 \mu\text{m}$ located on the PCS, smaller than the lateral extent of the photonic crystal, and an angular dispersion $\Delta\theta = \arctan(\lambda/\pi w_0) = 7.1 \times 10^{-3}$ rad that has a negligible influence on the optical properties of the PCS. A motorized Littman-Metcalf stabilized diode laser system from Sacher GmbH (Lion TEC-520) is used to probe the cavity. The cavity transmission is monitored with an avalanche photodiode (Thorlabs APD110C), and recorded continuously while the laser frequency is scanned over 4.8 nm. Simultaneously, the fringes of an imbalanced fiber interferometer are counted by a digital system (based on an Arduino micro-controller [27]) to measure the laser frequency in real time. The free

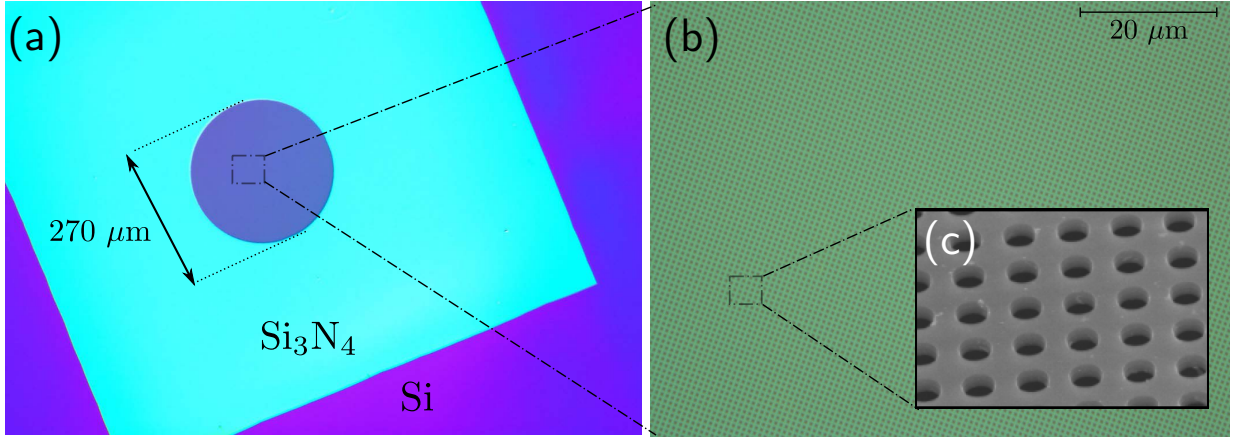


FIG. 1. (a) Optical image of the PCS made of a high-stress Si_3N_4 membrane suspended on a Si frame. The disk in the centre is the photonic crystal. (b) Optical microscope image of the PCS. (c) Scanning electron micrograph of the PCS.

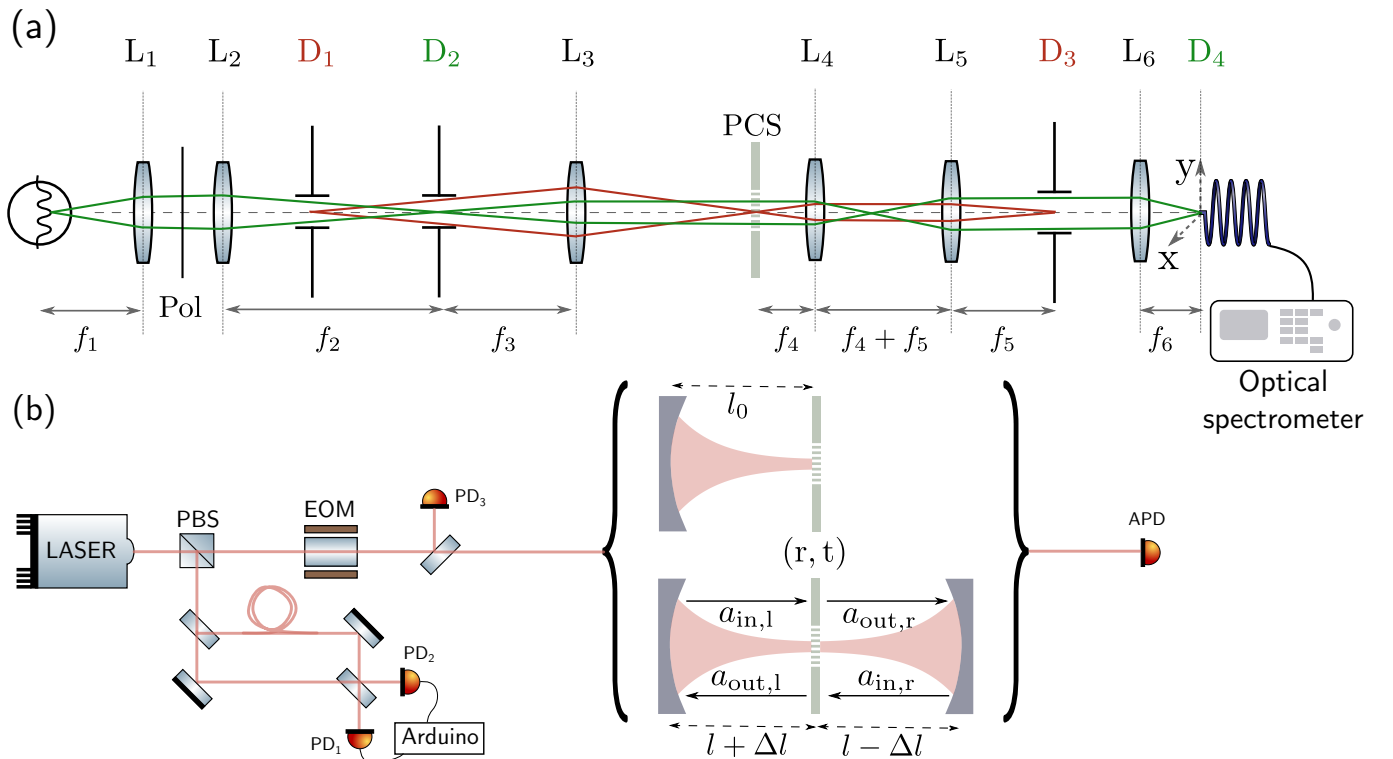


FIG. 2. (a) Setup used to record the PCS band structure. The light source is a Thorlabs tungsten halogen white lamp (SLS201). The illumination system is made of three lenses (L_1 , L_2 , L_3) and two diaphragms (D_1 , D_2). The imaging system is made of one microscope objective (L_4), two lenses (L_5 , L_6) and two diaphragms (D_3 , D_4), (D_4) being the fiber tip which can be scanned along the x and y directions. (Pol) is a linear polarizer and (PCS) is the photonic-crystal sample. The green rays are the Fourier image rays whereas the red rays are the real image rays. (b) Fabry-Perot cavity setups used to measure the membrane reflectivity and losses: the transmission of the cavity is measured by an avalanche photodiode (APD), and normalized by the incident signal from the photodiode (PD_3). For the single-ended cavity measurement (top cavity and Fig. 4), the laser diode is continuously scanned while an imbalanced interferometer is used to monitor its wavelength (PD_1 , PD_2), and 50-MHz sidebands are generated by an electrooptic modulator (EOM). For the membrane-in-the-middle measurement (bottom cavity and Fig. 5), the laser wavelength and membrane positions are scanned by piezoelectric actuators on the grating of the Littmann-Metcalf laser system and on the membrane mount respectively. (PBS): Polarizing Beam Splitter.

spectral range, bandwidth and visibility of each peak are extracted from Lorentzian fits.

Description and characterization of the PCS losses

In the following we provide a complete theoretical description of the PCS optical properties in the presence of losses. The membrane can be described by its scattering matrix, transforming the fields $a_{in,l}, a_{in,r}$ incoming from left and right into outgoing fields $a_{out,l}, a_{out,r}$ (see Fig. 2b):

$$\begin{pmatrix} a_{out,l} \\ a_{out,r} \end{pmatrix} = S \begin{pmatrix} a_{in,l} \\ a_{in,r} \end{pmatrix}, \quad (1)$$

$$\text{with } S = \begin{pmatrix} r & \bar{t} \\ t & \bar{r} \end{pmatrix} = \begin{pmatrix} r & t \\ t & r \end{pmatrix}, \quad (2)$$

where the symmetry of the membrane with respect to the xOy plane is used to assume that the direct (r, t) and reciprocal (\bar{r}, \bar{t}) complex reflection and transmission amplitudes are equal. The previous assumption allows S to be diagonalized

$$S = V \begin{pmatrix} r+t & 0 \\ 0 & r-t \end{pmatrix} V^{-1},$$

with the change of basis

$$V = \frac{1}{\sqrt{2}} \begin{pmatrix} 1 & 1 \\ 1 & -1 \end{pmatrix}$$

For a lossless membrane, S is unitary ($|r+t| = |r-t| = 1$), such that within a global phase factor, it is entirely determined by a single real parameter, for instance the intensity transmission $T = |t|^2$. However, in the presence of losses, the scattered fields have a total intensity smaller than the input fields and both eigenvalues obey

$$|r+t| \leq 1 \quad (3)$$

$$|r-t| \leq 1. \quad (4)$$

Three real parameters (plus a global phase term) are required to fully describe S : in addition to the intensity transmission T , we introduce the optical losses

$$L_{\pm} = 1 - |r \pm t|^2 \quad (5)$$

associated to the symmetric and antisymmetric combinations of left and right incoming fields $\begin{pmatrix} a_{in,l} \\ a_{in,r} \end{pmatrix} \propto \frac{1}{\sqrt{2}} \begin{pmatrix} 1 \\ \pm 1 \end{pmatrix}$. To obtain a measurement of L_{\pm} , the membrane can be positioned in the centre of a high-finesse cavity. This setup, initially proposed in the group of J. Harris [28], consists of two single-ended cavities coupled via the transmission of the membrane. If the input and output mirrors have the same amplitude reflectivity r' and if both sub-cavities have the same

length l , one gets in the absence of fields incident from outside the cavity (see Fig. 2b):

$$a_{in,l} = tr'e^{-2ikl}a_{in,r} + rr'e^{-2ikl}a_{in,l} \quad (6)$$

$$a_{in,r} = tr'e^{-2ikl}a_{in,l} + rr'e^{-2ikl}a_{in,r}, \quad (7)$$

where $k = \tilde{\omega}/c$ is the wave-number of the propagating field. The eigenmodes of the total optical cavity correspond to non-trivial solutions of this system for complex angular frequencies $\tilde{\omega}$. By taking the sum and difference of the previous equations, we obtain

$$a_{in,l} + a_{in,r} = (r+t)r'e^{-2ikl} [a_{in,l} + a_{in,r}] \quad (8)$$

$$a_{in,l} - a_{in,r} = (r-t)r'e^{-2ikl} [a_{in,l} - a_{in,r}]. \quad (9)$$

Non-trivial solutions of this system correspond to symmetric (+) (respectively antisymmetric (-)) modes with angular frequency $\omega_{p,+}$ (resp. $\omega_{p,-}$) and damping (full width at half maximum) γ_+ (resp. γ_-) given by

$$\omega_{p,\pm} = \text{Re}(\tilde{\omega}_{p,\pm}) = -\frac{c}{2l} (\arg[(r \pm t)r'] + 2p\pi) \quad (10)$$

$$\gamma_{\pm} = -2\text{Im}(\tilde{\omega}_{p,\pm}) = -\frac{c}{l} \log(|r \pm t||r'|) \quad (11)$$

where p is an integer corresponding to the longitudinal mode number. From Eq. (10), the frequency splitting between symmetric and antisymmetric modes of identical longitudinal numbers is given by:

$$\Delta\nu = \frac{\omega_{p,+} - \omega_{p,-}}{2\pi} = \frac{c}{4\pi l} \arg\left(\frac{r-t}{r+t}\right) \quad (12)$$

Finally, if the membrane losses L_{\pm} and mirror losses $L' = 1 - |r'|^2$ are small, Eq. (11) simplifies to

$$\gamma_{\pm} \approx \frac{c}{2l} (L_{\pm} + L').$$

Hence, the damping of the symmetric and antisymmetric modes gives direct access to the two parameters L_+ and L_- .

To perform this measurement, a 32-mm long cavity is formed by two mirrors with transmission-limited losses $L' = 455$ ppm, and radii of curvature 20 mm. The PCS is set in the centre of the cavity, on a three-axis translation stage. In order to align the cavity axis with respect to the PCS, the end mirror is also mounted on a two-axis translation stage. Finally, the PCS frame is glued on a piezoelectric stack to allow for automatic scans of its z position over several free spectral ranges.

RESULTS AND DISCUSSION

A. Band diagram of the PCS

The physics of high contrast gratings has previously been described in detail [30, 31]. Here, we extend it to

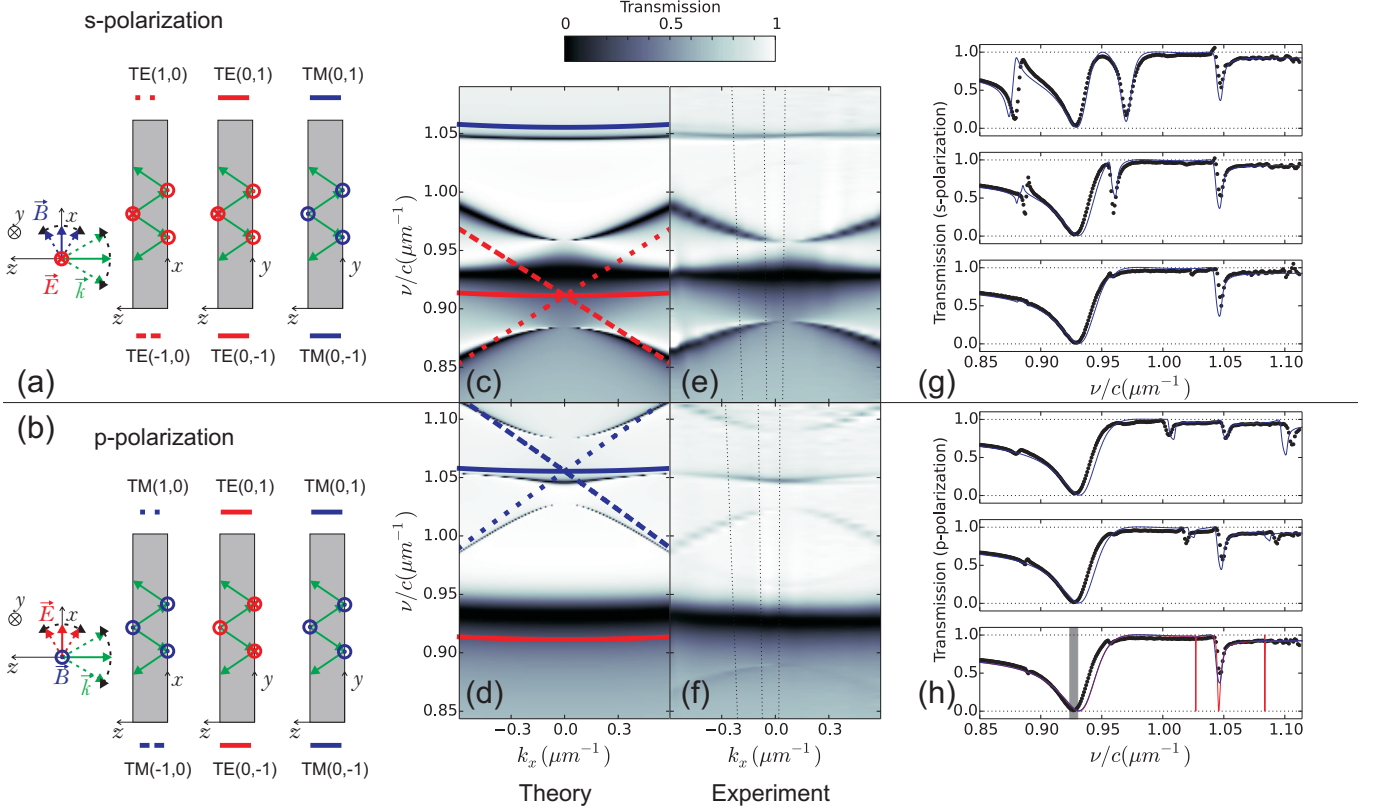


FIG. 3. (a),(b) First-order guided modes of an unpatterned membrane illuminated under s-polarization and p-polarization respectively. (c), (d) Theoretical reflectivity map of a 213 nm thick PCS patterned with a square lattice of period $\Lambda = 830$ nm, round hole filling factor $\eta = 30.6\%$, and dielectric constant given by [29], as a function of lateral wave-vector k_x , and normalized laser frequency ν/c under s-illumination (c), and p-illumination (d). The guided-resonance frequencies of the unpatterned membrane are superimposed, with TE-modes in red and TM-modes in blue (see (a) and (b) for the list of symbols). (e), (f) Experimental map of the reflectivity measured under s-illumination (e) and p-illumination (f). (g), (h) Experimental transmission (points) measured for an angle 3.57° , 1.23° and 0.33° (from top to bottom) for s-illumination (g) and p-illumination (h). The dashed lines of constant $k_x/k_{z,\text{air}}$ in (e) and (f) correspond to these measurements. The convoluting theoretical RCWA fit convoluted with the spectrometer response is plotted as a blue line. As an example, the unconvoluted RCWA result is plotted in red in the last cut of (h). In this plot, the width of the shaded area corresponds to the wavelength span scanned around the TE resonance in Fig. 4.

the case of a PCS, following from earlier work [13, 32]. The high-reflection properties of the PCS result from Fano resonances arising from an interference between the direct reflection from the PCS and light leaking out from internal high-Q guided modes in the PCS. To unveil the band structure of the guided modes, we calculate the transmission of the PCS by means of the Rigorous Coupled Wave Analysis (RCWA) [33] which is well suited to periodic structures such as our square lattice of holes (lattice parameter $\Lambda = 830$ nm, membrane thickness $h = 213$ nm, hole radius $r_h = 276$ nm). We begin the analysis with the unpatterned membrane limit for which the dielectric constant of both the membrane material and the holes is set to an average value $\epsilon_{\text{eff}} = \eta\epsilon_{\text{air}} + (1 - \eta)\epsilon_{\text{Si}_3\text{N}_4} = 2.95$. The field solutions are guided modes, referred to as “unperturbed modes” in the following discussion. They are plane waves re-

flected by total internal reflection upon the two faces of the membrane. In this regime, the unperturbed modes are evanescent outside of the membrane: the z component of their wavevector fulfils $k_{z,m} \in \mathbb{R}^+$ inside the membrane, and $k_{z,\text{air}} \in i\mathbb{R}^-$ in the surrounding medium. TE (TM) modes have their electric (magnetic) field within the plane of the membrane, and are represented on Fig. 3 in red (blue) respectively. The eight modes are sorted according to their symmetry class with respect to the xOz plane. Symmetric modes ($TM(\pm 1, 0)$) are not excited under s-illumination whereas antisymmetric modes ($TE(\pm 1, 0)$) are not excited under p-illumination. The complex coefficients describing the reflection inside the membrane for the electric field are given by Fresnel’s law

$$r_{\text{TM}} = \frac{k_{z,m} - \epsilon_{\text{eff}}k_{z,\text{air}}}{k_{z,m} + \epsilon_{\text{eff}}k_{z,\text{air}}}, \quad r_{\text{TE}} = \frac{k_{z,\text{air}} - k_{z,m}}{k_{z,m} + k_{z,\text{air}}}.$$

We have numerically solved the round-trip resonance condition within the membrane

$$r_j^2 e^{-2ik_{z,m}h} = 1, \quad (13)$$

for $j = TE$ or TM , and for the lowest possible value of $\omega = c\sqrt{(k_x + 2p_x\pi/\Lambda)^2 + (2p_y\pi/\Lambda)^2 + k_{z,m}^2}$, (where $(p_x, p_y) = (\pm 1, 0)$ or $(0, \pm 1)$ are the diffraction orders in the x and y directions respectively). Note that the periodicity Λ is not a property of the unpatterned membrane and that it is arbitrarily chosen to match that of the patterned membrane. Given the phases of r_{TE} and r_{TM} , we find that TE modes have a lower fundamental resonance frequency than TM modes. Finally, the symmetry of the mode with respect to the xOy plane is given by the sign of the half round-trip propagation coefficient

$$r_j e^{-ik_{z,m}h} = \pm 1. \quad (14)$$

From the expressions of r_{TE} and r_{TM} , it follows that the fundamental TE (resp. TM) mode is antisymmetric (symmetric) with respect to xOy . The calculated mode frequencies as a function of transverse wavevector k_x are represented by the lines in Fig. 3c and d. To first order, the frequency of the modes diffracted along the y direction is not affected by the transverse k_x component, contrary to the modes diffracted along the x direction.

The results of the RCWA for the patterned membrane are superimposed as a color plot in Fig. 3c and d (refractive index of Si_3N_4 given by [29]). In this case, the modes described in the unpatterned case are now coupled together by diffraction, giving rise to avoided crossings. In addition, the reflections at the membrane/air interfaces couple the guided modes to the zeroth-order modes propagating in free-space, leading to an effective loss channel. The guided resonances acquire a finite lifetime inversely proportional to the width of the Fano resonance (cut along a fixed value of k_x in Fig. 3). We find that the lifetime of TM modes is approximately 20 times that of TE modes. Note that at normal incidence the yOz plane constitutes an additional plane of (anti)-symmetry in the s- (p-) polarization, and hence, only the combinations $TE(1, 0) + TE(-1, 0)$ and $TM(0, 1) + TM(0, -1)$ (resp. $TE(0, 1) + TE(0, -1)$ and $TM(1, 0) + TM(-1, 0)$) are effectively coupled to free space modes: the linewidth of the other Fano resonances vanish close to $k_x = 0$. The white light angle-resolved spectrometer described previously allowed us to measure the band structure of guided modes for small transverse wave-vectors k_x . The experimental transmissions with s- (p-) illumination is presented in Fig. 3e and 3f, together with 3 different cuts with incidence angle 3.57° , 1.23° and 0.33° . The simulation is fitted to the data with the hole radius and membrane thickness as free parameters. Indeed, the former is only specified to within 10 % accuracy and the latter may differ from the design value due to imperfect

pattern transfer upon electron-beam lithography and etching.

The fitted values $r_h = 276$ nm and $h = 213$ nm are in good agreement with the design values. The theoretical fits are represented in blue in Fig. 3g and h. The reduced visibility of the peaks, particularly pronounced with TM modes, is well accounted for by convolving the theoretical map with the 4-nm wide response of the spectrometer. In the next section, we analyse in more detail the TE Fano resonance responsible for the largest dip in transmission close to $\nu = c \times 0.929 \mu\text{m}^{-1} = c/(1.076 \mu\text{m})$ in Fig. 3g and h.

B. Detailed characterization of a Fano resonance

For optical frequencies $\nu = c/\lambda$ close to a guided mode resonance, the PCS complex reflection and transmission coefficients r and t are given in good approximation by the simple two-mode model [32]

$$r(\lambda) = r_d \pm \frac{\gamma}{i(\lambda - \lambda_0) + \gamma} (\pm r_d - t_d) \quad (15)$$

$$t(\lambda) = t_d + \frac{\gamma}{i(\lambda - \lambda_0) + \gamma} (\pm r_d - t_d), \quad (16)$$

where r_d and t_d are the off-resonant coefficients ($|r_d + t_d| = |r_d - t_d| = 1$), λ_0 is the wavelength of the guided mode resonance, γ the resonance width, and the plus/minus sign in Eq. (15) reflects the symmetry of the guided mode: as discussed in the previous section, the lowest order TE-mode is antisymmetric with respect to the xOy plane, and thus the minus sign applies. In the absence of optical losses, a striking feature of this Fano lineshape is the existence of a frequency $\lambda_1 = \lambda_0 + i\gamma r_d/t_d$ for which the PCS transmission vanishes: $T(\lambda_1) = |t(\lambda_1)|^2 = 0$, and accordingly, the reflectivity tends to unity: $R(\lambda_1) = |r(\lambda_1)|^2 = 1$.

By fitting the RCWA results with Eqs. 15 and 16 around the largest TE Fano resonance, we determine $\lambda_1 = 1076$ nm and $\gamma = 12$ nm. In order to study the optical behaviour of the PCS around λ_1 , a single-ended optical cavity of length l_0 was realized, using the PCS as end-mirror (see Fig. 2). The transmission of the cavity is monitored while a tunable diode laser is swept across the Fano resonance. The recorded signal, shown in Fig. 4a, displays a comb of peaks spaced by the free spectral range of the cavity given by

$$\Delta\lambda_{\text{FSR}} = \frac{\lambda_0^2}{2l_0}. \quad (17)$$

The linewidth $\Delta\lambda_n(\lambda)$ of each longitudinal cavity mode n is then obtained by fitting a Lorentzian profile to each of the individual peaks. To minimize the impact of scan speed fluctuations, we generate 50-MHz sidebands in the laser spectrum with an electro-optic modulator, used as a frequency calibration of the instantaneous scanning speed. Denoting the finesse of the cavity

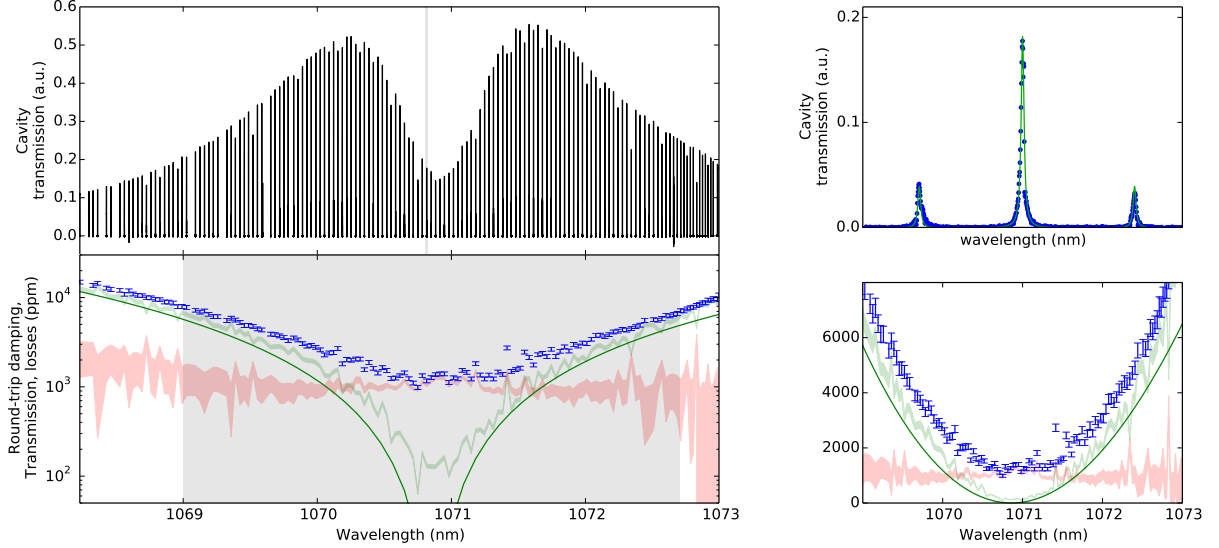


FIG. 4. (a) Transmission of a single-ended cavity as a function of laser wavelength. (b) Zoom of an individual Airy peak, showing modulation sidebands, and a Lorentzian fit. (c) Round-trip loss inferred from the fits of individual Airy peaks in blue. The error bars are extracted from the average off-centering of the central peak between left and right sidebands. The red and green shaded area represents the confidence interval for the PCS loss and transmission respectively. The green line is the theoretical transmission calculated by RCWA with the same parameters as Fig. 3, except for $r_h = 285$ nm (this experiment uses a second membrane from the same micro-fabrication run). (d) provides a linear representation of the data in (c).

by $\mathcal{F}(\lambda)$, the total round-trip loss of the cavity is given by $\Gamma_{\text{RTL}}(\lambda) = 2\pi/\mathcal{F}(\lambda) = 2\pi\Delta\lambda_n(\lambda)/\Delta\lambda_{\text{FSR}}(\lambda)$. They are plotted in blue in Fig. 4b as a function of the laser wavelength. The lowest level of $\Gamma_{\text{RTL}} = (985 \pm 25)$ ppm, corresponding to a finesse $\mathcal{F}(\lambda_1) = 6385 \pm 150$, was found at $\lambda_1 = 1070.9$ nm. The 5.1 nm discrepancy with respect to the results of Fig. 3 is quite small considering that two different membranes from the same micro-fabrication run were used in these experiments. In the simulations, it is accounted for by changing the hole radius from $r_h = 276$ nm to $r_h = 285$ nm. Taking into account the 455 ppm transmission of the input mirror, we infer a membrane reflectivity as good as $1 - R(\lambda_1) = 530$ ppm.

To discriminate between the contributions of the membrane transmission $T(\lambda) = |t(\lambda)|^2$ and the optical losses $L(\lambda) = 1 - R(\lambda) - T(\lambda)$ in $\Gamma_{\text{RTL}}(\lambda)$, we use the extra-information embedded in the height of the transmitted peaks. Indeed, the transmission $\mathcal{T}_n(\lambda)$ of the cavity at resonance with the n^{th} mode is given by

$$\mathcal{T}_n(\lambda) = \frac{4T_c T(\lambda)}{\Gamma_{\text{RTL}}(\lambda)^2}, \quad (18)$$

where T_c is the transmission of the input mirror, assumed to be constant over the wavelength range scanned here. In the experiment, a signal proportional to $\mathcal{T}_n(\lambda)$ is measured, so that we can deduce $T(\lambda)$ from Eq. (18) within a multiplicative constant α . By assuming that

the losses $L(\lambda)$ are within the interval $[0, \Gamma_{\text{RTL}}(\lambda_1)]$ at the highest accessible wavelength, we obtain a confidence interval for α , and hence for $T(\lambda) = \Gamma_{\text{RTL}}(\lambda) - L(\lambda)$ (in green on Fig. 4c and d) and for $L(\lambda)$ (in red) over the whole wavelength range. For comparison, the transmission calculated by RCWA is displayed with a green solid line on Fig. 4c and d. The agreement between RCWA and experimental results is excellent. At the Fano resonance $\lambda_1 = 1070.9$ nm, the round-trip damping is vastly dominated by membrane losses. The lowest cavity bandwidth $\kappa/2 = c/4l\mathcal{F}(\lambda_1) = 675$ kHz measured in this single-ended cavity setup approaches the resolved-sideband condition for first-order flexure modes of the suspended membrane.

To understand the exact form of the scattering matrix, and gain insight on the origin of the losses observed in the previous experiment, a PCS is positioned in the middle of a high-finesse cavity. The PCS is scanned along the cavity axis with a piezoelectric actuator. In this configuration, the PCS couples two cavities of length $l_1 + \Delta l/2$, and $l_2 - \Delta l/2$, where $l_1 \approx l_2 \approx l$ are the initial lengths of the first and second sub-cavities, supposed to be simultaneously resonant with the central laser wavelength λ_c for $\Delta l = 0$. The cavity transmission, recorded as a function of Δl and laser detuning $\delta\nu \propto \lambda_c - \lambda$, is represented in the color plots of Fig. 5a, b and c. The avoided crossing of symmetric and antisymmetric modes is visible in the centre of the figure. From

a Lorentzian fit of the peaks at the avoided crossing and along the vertical axis, we extract the frequency spacing $\Delta\nu$, and the linewidth γ_{\pm} of symmetric and antisymmetric modes. The experiment is then reproduced for several laser wavelengths λ_c close to the Fano resonance and the corresponding frequency spacings and linewidths are shown in Fig. 5d and e respectively.

In Fig. 5a and c, the upper and lower branches of the avoided crossing are strongly asymmetric. This is a direct consequence of the difference between L_+ and L_- . For $\lambda_c < \lambda_1$ (Fig. 5a), the phase of $(r - t)/(r + t)$ is positive, such that from Eq. (12), the symmetric mode (angular frequency ω_+) constitutes the upper branch of the crossing, while the antisymmetric mode (angular frequency ω_-) is the lower branch. On the other hand, for $\lambda_c > \lambda_1$ (Fig. 5c), $\Delta\nu = (\omega_+ - \omega_-)/2\pi$ changes its sign and the upper and lower branches are exchanged. Finally, at the Fano resonance $\lambda_c = \lambda_1$, r and t are in phase, so that symmetric and antisymmetric modes are perfectly degenerate. Combined with the inequalities of Eq. (3), an upper bound for the transmission of the membrane can be derived: $|t| \leq 1 - |r|$ at the Fano resonance. For $1 - R = 985$ ppm, this corresponds to a transmission as low as $T \leq 0.2$ ppm. Hence, the residual transmission of 100 ppm observed in Fig. 4 is somehow in contradiction with the two-port description developed in this work. A first explanation is the possible scattering into non-overlapping spatial modes due to surface roughness. Moreover, given our experimental parameters, we expect from RCWA that the wavevector components of the input Gaussian beam not aligned with a symmetry plane of the membrane should give rise to ≈ 20 ppm transmission into the polarization orthogonal to the input beam (with a spatial wavefunction that is antisymmetric with respect to the xOz and yOz planes). Nevertheless, as visible on Fig. 4, the residual transmission only accounts for a small fraction of the total cavity losses close to the Fano resonance, and the nature of these losses still needs to be elucidated.

The difference between the losses L_{\pm} experienced by the symmetric and antisymmetric modes is well captured by a simple phenomenological model: since the Fano resonance results from the interference between the direct PCS transmission and a high-Q guided resonance, it can be safely assumed that the losses mostly affect the former. Hence, Eqs. (15) and (16) are modified to include a phenomenological loss rate γ' to the high-Q response as

$$r = r_d - \frac{\gamma}{i(\lambda - \lambda_0) + \gamma + \gamma'}(-r_d - t_d)$$

$$t = t_d + \frac{\gamma}{i(\lambda - \lambda_0) + \gamma + \gamma'}(-r_d - t_d).$$

Using this model, it follows that

$$L_+ = 0 \quad (19)$$

$$L_- = \frac{4\gamma\gamma'}{(\gamma + \gamma')^2 + (\lambda - \lambda_0)^2}, \quad (20)$$

and thus, only the antisymmetric mode of the two-cavity setup is affected by the optical losses, with a value proportional to the Lorentzian response of the guided resonance. This is an intuitive result since the antisymmetric guided resonance under study isn't driven by a symmetric incoming field (this would be vice-versa for the symmetric TM resonance). To quantitatively evaluate the model, Fig. 5e shows the total expected linewidths $L_{\pm} + L'$, where $\gamma' = 1.0 \times 10^{-2}$ nm is the only adjustable parameter, since $\lambda_1 = 1079.1$ nm, $\gamma = 12$ nm and $L' = 455$ ppm are independently determined. Therefore, optical losses are found to account for less than 0.1 % in the total decay rate of the guided mode resonance. The previous model shows that the asymmetry between L_+ and L_- is a direct consequence of the physics of Fano resonances, and that it is not specific to a particular loss mechanism such as absorption or scattering, since both would preferentially affect the high-Q guided mode. This finding is in stark contradiction with a model recently proposed in [21], where such an asymmetry was attributed to absorption in the material. Moreover, we show in the following that absorption should have a negligible influence on the optical loss of our PCS. Indeed, if the losses observed in this experiment were entirely due to optical absorption, the value $\text{Im}(n) = (3.5 \pm 1.5) \times 10^{-5}$ could be derived for the absorption of the Si_3N_4 layer. The values of $L_{\pm} + L'$ obtained with a RCWA simulation including an absorption $2 \times 10^{-5} \leq \text{Im}(n) \leq 5 \times 10^{-5}$ are located within the shaded areas in Fig. 5e. Since previous experiments [34] have found values for the absorption of a similar layer an order of magnitude smaller ($\text{Im}(n) = 2.0 \times 10^{-6}$), we conclude that scattering is still the main source of losses. In the single-ended cavity case where the field is essentially incident on one side of the membrane, the relevant optical losses are given by $L = (L_+ + L_-)/2$. Thus, the decrease of optical losses with optical wavelength visible in Fig. 4b is consistent with Eq. 19 and 20. With the previous smaller value of Si_3N_4 absorption, a RCWA simulation shows that a reflectivity as high as $R \approx 1 - 80$ ppm, corresponding to a finesse close to 80 000, could be achieved by improving the PCS fabrication process.

CONCLUSIONS

High-stress Si_3N_4 films have been successfully patterned to realize a 2D photonic crystal slab. We have provided a detailed study of the rich mode structure underlying the high-reflectivity of the crystal and have fully characterized the scattering and loss properties of the

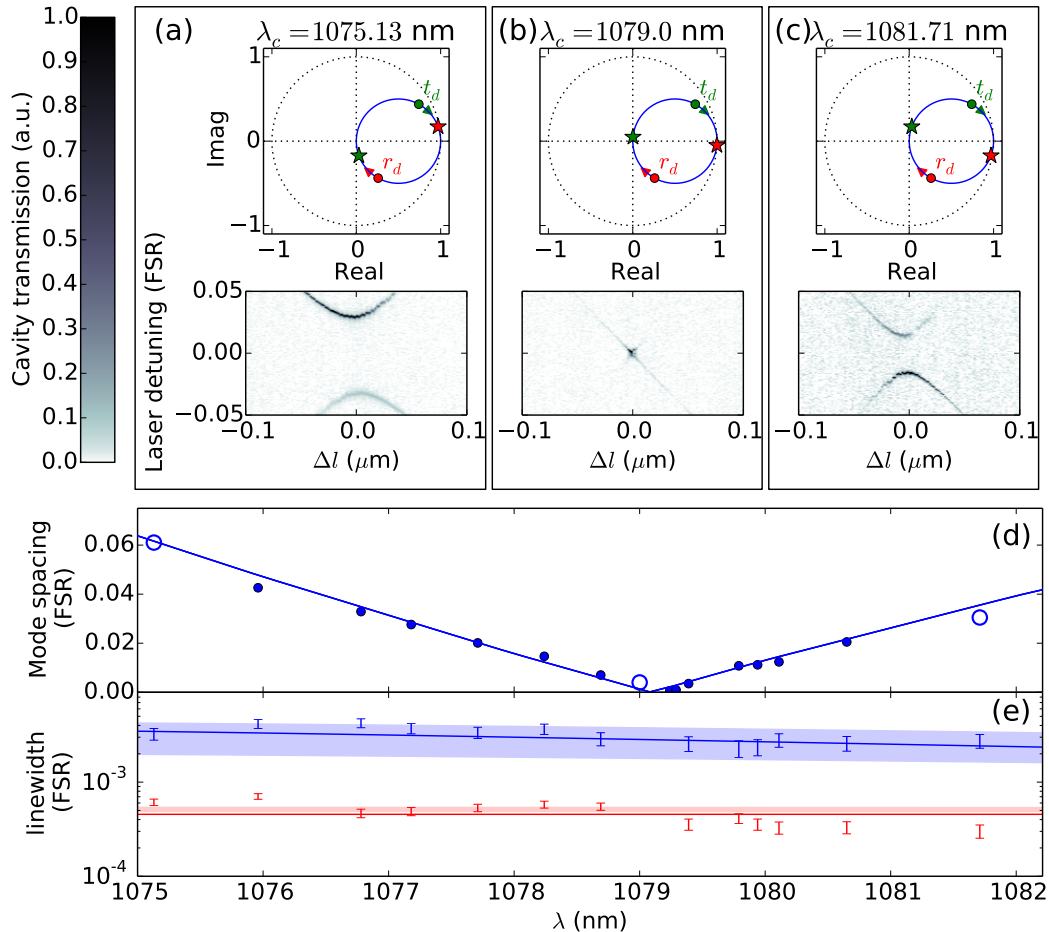


FIG. 5. (a), (b) and (c) show colorplots of the cavity transmission versus the cavity length and laser detuning with respect to three different laser central wavelengths λ_c . Above are the corresponding complex representations of $r(\lambda)$ and $t(\lambda)$, where a global phase factor has been applied to ensure that $r(\lambda_1) = r_d + t_d = 1$. The green and red bullets correspond to $r(\lambda_0) = t_d$ and $t(\lambda_0) = r_d$ respectively, the green and red stars correspond to $t(\lambda_c)$ and $r(\lambda_c)$ respectively. In (a) ((c)), λ_c is chosen smaller (larger) than λ_1 . In (b), λ_c is chosen very close to λ_1 , so that $r(\lambda_c) \simeq 1$ and $t(\lambda_c) \simeq 0$. (d) Mode frequency spacing for $\Delta l = 0$. A minimum is reached for $\lambda = \lambda_1$. The blue line corresponds to the mode spacing calculated by RCWA using Eq. (12) (same parameters as in Fig. 3 and 4, except for $r_h = 272$ nm). (e) Linewidths of the two modes. The blue strip represents the value obtained with RCWA simulations including an absorption of $2 \times 10^{-5} \leq \text{Im}(n) \leq 5 \times 10^{-5}$. Optical detunings are normalized by the FSR of the sub-cavities $\Delta\lambda_{\text{FSR}} = \lambda_c^2/2l$. The error bars are inferred from the variation of the fit parameters obtained with neighbouring values of Δl .

device. We have also experimentally demonstrated the wide tunability of the membrane reflectivity, via the adjustment of the laser wavelength close to a Fano resonance. Such tunability is highly desirable in the context of membrane-in-the-middle optomechanics experiments. In particular, the ability to reach very narrow energy gap between the eigenmodes of the coupled cavities could be used to enter the regime where the photon exchange time becomes comparable to the mechanical period. This would enable the observation of mechanically-induced coherent photon dynamics, like Autler-Townes splitting or Landau-Zener-Stueckelberg dynamics [35]. Finally, the

bandwidth of the single-ended cavity described in this work, as low as 675 kHz sets us in the resolved sideband regime for the first order harmonics of the drum mode, ranging from 596 kHz for the (0, 1) mode to 1.2 MHz for the (2, 2) mode used in previous quantum optomechanics experiments [16]. Hence, this technique results in devices already suitable for the development of optomechanical transducers.

ACKNOWLEDGEMENTS

The authors gratefully acknowledge M. Corcos, I. Krasnokutskaya, X. Pennehouat and L. Pinol for preliminary experimental developments. We thank J. Palomo and M. Rosticher for developing the first steps of the microfabrication process. Finally, we thank J. Lawall and R. Guérout for insightful scientific discussions. This research has been partially funded by the Agence Nationale de la Recherche programs “ANR-2011-BS04-029 MiNO-ToRe” and “ANR-14-CE26-0002 QuNaT”, the Marie Curie Initial Training Network “cQOM”, and the DIM nano-K Ile-de-France program “NanoMecAtom”. S. C. is supported by the Marie Skłodowska-Curie Individual Fellowship program.

* Current affiliation: IBM Research - Zürich, Säumerstrasse 4, 8803 Rüschlikon, Switzerland

- [1] Zhou W, Zhao D, Shuai YC, Yang H, Chuwongin S, Chadha A, et al. Progress in 2D photonic crystal Fano resonance photonics. *Prog Quantum Electron.* 2014;38(1):1–74. Available from: <http://dx.doi.org/10.1016/j.pquantelec.2014.01.001>.
- [2] Lin C, Lu Z, Shi S, Jin G, Prather DW. Experimentally demonstrated filters based on guided resonance of photonic-crystal films. *Appl Phys Lett.* 2005;87(9).
- [3] Yacomotti AM, Raineri F, Vecchi G, Monnier P, Raj R, Levenson A, et al. All-optical bistable band-edge Bloch modes in a two-dimensional photonic crystal. *Appl Phys Lett.* 2006;88(23):2004–2007.
- [4] Magnusson R, Wawro D, Zimmerman S, Ding Y. Resonant photonic biosensors with polarization-based multiparametric discrimination in each channel. *Sensors.* 2011;11(2):1476–1488.
- [5] Yang W, Adair Gerke S, Wei Ng K, Rao Y, Chase C, Chang-Hasnain CJ. Laser optomechanics. *Sci Rep.* 2015;5:13700. Available from: <http://www.nature.com/doi/10.1038/srep13700>.
- [6] Yanik MF, Fan S. Stopping and storing light coherently. *Phys Rev A - At Mol Opt Phys.* 2005;71(1):1–10.
- [7] Yacomotti AM, Monnier P, Raineri F, Ben Bakir B, Seassal C, Raj R, et al. Fast thermo-optical excitability in a two-dimensional photonic crystal. *Phys Rev Lett.* 2006;97(14):6–9.
- [8] Friedrich D, Barr BW, Brückner F, Hild S, Nelson J, Macarthur J, et al. Waveguide grating mirror in a fully suspended 10 meter Fabry-Perot cavity. *Opt Express.* 2011 aug;19(16):14955–63. Available from: <http://www.ncbi.nlm.nih.gov/pubmed/21934857>.
- [9] Gavartin E, Braive R, Sagnes I, Arcizet O, Beveratos A, Kippenberg TJ, et al. Optomechanical Coupling in a Two-Dimensional Photonic Crystal Defect Cavity. *Phys Rev Lett.* 2011 may;106(20):203902. Available from: <http://link.aps.org/doi/10.1103/PhysRevLett.106.203902>.
- [10] Alegre TPM, Safavi-Naeini A, Winger M, Painter O. Quasi-two-dimensional optomechanical crystals with a complete phononic bandgap. *Opt Express.* 2011;19:5658–5669. Available from: <http://www.ncbi.nlm.nih.gov/pubmed/20028887>.
- [11] Kemiktarak U, Metcalfe M, Durand M, Lawall J. Mechanically compliant grating reflectors for optomechanics. *Applied Physics Letters.* 2012;100:061124. Available from: <http://scitation.aip.org/content/aip/journal/apl/100/6/10.1063/1.3684248>.
- [12] Bui CH, Zheng J, Hoch SW, Lee LYT, Harris JGE, Wei Wong C. High-reflectivity, high-Q micromechanical membranes via guided resonances for enhanced optomechanical coupling. *Appl Phys Lett.* 2012;100(2):021110. Available from: <http://link.aip.org/link/APPLAB/v100/i2/p021110/s1?Agg=doi>.
- [13] Makles K, Antoni T, Kuhn AG, Deléglise S, Briant T, Cohadon PF, et al. 2D photonic-crystal optomechanical nanoresonator. *Opt Lett.* 2015;40:174–177. Available from: <http://ol.osa.org/abstract.cfm?URI=ol-40-2-174>.
- [14] Andrews RW, Peterson RW, Purdy TP, Cicak K, Simmonds RW, Regal CA, et al. Bidirectional and efficient conversion between microwave and optical light. *Nat Phys.* 2014;10(April):321–326. Available from: <http://dx.doi.org/10.1038/nphys2911>.
- [15] Bagci T, Simonsen A, Schmid S, Villanueva LG, Zeuthen E, Appel J, et al. Optical detection of radio waves through a nanomechanical transducer. *Nature.* 2014 mar;507(7490):81–5. Available from: <http://www.ncbi.nlm.nih.gov/pubmed/24598636>.
- [16] Purdy TP, Peterson RW, Regal CA. Observation of Radiation Pressure Shot Noise on a Macroscopic Object. *Science.* 2013 sep;339:801. Available from: <http://arxiv.org/abs/1209.6334>.
- [17] Reinhardt C, Müller T, Bourassa A, Sankey JC. Ultralow-Noise SiN Trampoline MEMS for Sensing and Optomechanics. 2015;p. 7. Available from: <http://arxiv.org/abs/1511.01769>.
- [18] Norte RA, Moura JP, Gröblacher S. Mechanical Resonators for Quantum Optomechanics Experiments at Room Temperature. *Phys Rev Lett.* 2015; Available from: <http://arxiv.org/abs/1511.06235>.
- [19] Yuan M, Cohen MA, Steele GA. Silicon nitride membrane resonators at millikelvin temperatures with quality factors exceeding 108. *Applied Physics Letters.* 2015;107(26). Available from: <http://scitation.aip.org/content/aip/journal/apl/107/26/10.1063/1.4938747>.
- [20] Schliesser A, Riviere R, Anetsberger G, Arcizet O, Kippenberg TJ. Resolved-sideband cooling of a micromechanical oscillator. *Nat Phys.* 2008 may;4(5):415–419. Available from: <http://dx.doi.org/10.1038/nphys939>http://www.nature.com/nphys/journal/v4/n5/supinfo/nphys939/_s1.html.
- [21] Stambaugh C, Xu H, Kemiktarak U, Taylor J, Lawall J. From membrane-in-the-middle to mirror-in-the-middle with a high-reflectivity sub-wavelength grating. *Annalen der Physik.* 2014 oct;8:81–88. Available from: <http://doi.wiley.com/10.1002/andp.201400142>.
- [22] Qiang Z, Chen L, Yang H, Pang H, Ma Z, Zhou W, et al. Fano filter modal analysis based on transferred silicon nanomembranes on flexible substrates. *Proc SPIE Vol.* 2008;7031(2008):703109–1. Available from: <http://scholar.google.com/scholar?hl=en&btnG=Search&q=intitle:Fano+filter+modal+analysis+>

- based+on+transferred+silicon+nanomembranes+on+flexible+substrates{\#}0.
- [23] Singh Chadha A, Zhao D, Chuwongin S, Ma Z, Zhou W. Polarization- and angle-dependent characteristics in two dimensional photonic crystal membrane reflectors. *Appl Phys Lett*. 2013;103(21).
- [24] Stomeo T, Grande M, Raino G, Passaseo A, D'Orazio A, Cingolani R, et al. Optical filter based on two coupled PhC GaAs-membranes. *Opt Lett*. 2010;35(3):411–413.
- [25] Norcada;. www.norcada.com.
- [26] Purdy TP, Peterson RW, Yu PL, Regal CA. Cavity optomechanics with Si_3N_4 membranes at cryogenic temperatures. *New Journal of Physics*. 2012 nov;14:115021. Available from: <http://stacks.iop.org/1367-2630/14/i=11/a=115021?key=crossref.11356b3176442bddf1dcc4ae5ae5b3b0>.
- [27] Arduino;. www.arduino.cc/.
- [28] Thompson JD, Zwickl BM, Jayich aM, Marquardt F, Girvin SM, Harris JGE. Strong dispersive coupling of a high-finesse cavity to a micromechanical membrane. *Nature*. 2008 mar;452:72–5. Available from: <http://www.ncbi.nlm.nih.gov/pubmed/18322530>.
- [29] Dielectric permittivity of Si_3N_4 ; $\epsilon_{\text{Si}_3\text{N}_4} = 1 + 2.8939\lambda^2/(\lambda^2 - (0.13867\mu\text{m})^2)$. (from Ref. [36]).
- [30] Karagodsky V, Sedgwick FG, Chang-Hasnain CJ. Theoretical analysis of subwavelength high contrast grating reflectors. *Optics express*. 2010;18:16973–16988.
- [31] Karagodsky V, Chang-Hasnain CJ. Physics of near-wavelength high contrast gratings. *Optics Express*. 2012;20:10888.
- [32] Fan S, Joannopoulos J. Analysis of guided resonances in photonic crystal slabs. *Physical Review B*. 2002;65(23):235112. Available from: <http://link.aps.org/doi/10.1103/PhysRevB.65.235112>.
- [33] Liu V, Fan S. S 4: A free electromagnetic solver for layered periodic structures. *Computer Physics Communications*. 2012;183:2233–2244. Available from: <http://dx.doi.org/10.1016/j.cpc.2012.04.026>.
- [34] Serra E, Bawaj M, Borrielli A, Di Giuseppe G, Forte S, Kralj N, et al. Microfabrication of large area high-stress silicon nitride membranes for optomechanical devices. *arXiv*. 2015; Available from: <http://arxiv.org/abs/1601.02669>.
- [35] Heinrich G, Harris JGE, Marquardt F. Photon shuttle: Landau-Zener-Stückelberg dynamics in an optomechanical system. *Physical Review A*. 2010 jan;81:011801. Available from: <http://link.aps.org/doi/10.1103/PhysRevA.81.011801>.